Numerical simulation of natural convection and boil-off in a small size pressurized LNG storage tank

J.L. Ferrín[a,b,*], L.J. Pérez-Pérez[a,c]

[a] *Universidade de Santiago de Compostela, 15782 Santiago de Compostela, Spain*
[b] *Instituto Tecnológico de Matemática Industrial, 15782 Santiago de Compostela, Spain*
[c] *Instituto de Matemáticas, 15782 Santiago de Compostela, Spain*

Abstract

A numerical simulation of the flow of LNG stored in a small-sized cylindrical tank is presented. The main scope of this work is to characterize the heat ingress to the tank as well as the boil-off rate, depending on the filling level and the insulation layer thickness. The tank is assumed to be in a state of inactivity, such that the fluid phases are initially quiescent and are not released to the exterior. The proposed mathematical model consists of a conjugate heat transfer problem coupled with the SST $K-\omega$ turbulence model for the fluid phases. The free surface separating liquid and vapor in the tank is tracked using the Volume of Fluid method (VOF). The model is solved using the software ANSYS Fluent. It is shown that the filling level of the tank substantially influences the boiling rate and the degree of stratification, as well as the flow structures generated by free convection. The relation among the insulation thickness and total heat leak is established, showing that the obtained increased heat ingress due to lower insulation thickness values leads to a rise in pressurization and boil-off rates.

Keywords: Numerical Simulation, LNG, boil-off, natural convection, conjugate heat transfer.

1. Introduction

Natural gas is a fossil fuel mainly composed of methane, ethane and propane, with traces of heavier hydrocarbons and also a varying amount of nitrogen. Its composition is highly dependent on its origin. Usually, methane content is above 90%. Natural gas is currently the fastest-growing non-renewable source of energy [1] and is also expected to continue growing in the coming years, with a projected growth rate of 1.6% (see [2]). This is principally due to its cost being competitive and comparatively low compared to the historical one. Furthermore, it is cleaner than the remaining fossil alternatives, as its combustion produces substantially less carbon dioxide and also reduces the emissions of other highly contaminant gases, such as sulfur dioxide.

*Corresponding author
Email addresses: joseluis.ferrin@usc.es (J.L. Ferrín), luisjavier.perez@usc.es (L.J. Pérez-Pérez)

Nomenclature

Greek symbols

α	Volume fraction
β	Thermal expansion coefficient (K^{-1})
Δt	Time step size (s)
γ	Evaporation rate coefficient (s^{-1})
μ	Dynamic viscosity (Pa·s)
μ_T	Turbulent viscosity (Pa·s)
ω	Specific dissipation rate (s^{-1})
ρ	Density (kg/m^3)

Latin symbols

A_l	Wall surface area in contact with liquid (m^2)
c_p	Specific heat, at constant pressure (J/(kg·K))
E	Total specific energy (J/kg)
H_{vap}	Latent heat of vaporization (J/kg)
h	Heat transfer coefficient ($W/(m^2 \cdot K)$)
g	Gravitational acceleration (m/s^2)
M	Molar mass (kg/kmol)
m_l	Liquid mass (kg)
$\dot{m}_{lv}$	Mass transfer source term ($kg/(m^3 \cdot s)$)
$\mathbf{n}$	Outward-pointing unit normal vector (m)
K	Turbulent kinetic energy (m^2/s^2)
k	Thermal conductivity (W/(m·K))
k_T	Turbulent thermal conductivity (W/(m·K))
p	Pressure (Pa)
$\overline{q}_l$	Average heat flux, liquid phase (W/m^2)
Q	Total heat flux (W)
T	Temperature (K)
r	Radial coordinate (m)
R	Ideal gas constant (J/(mol·K))
T_R	Reference temperature (K)
T_{Rb}	Reference temperature (Boussinesq model) (K)
t	Time (s)
v	Specific volume (m^3/kg)
V_m	Molar volume (m^3/mol)
$\mathbf{v}$	Velocity (m/s)
w	Insulation layer thickness (mm)
y	Vertical coordinate (m)

Subscripts

$_c$	Critical property
$_f$	Fluid
$_l$	Liquid phase
$_p$	Perlite
$_s$	Solid
$_{sat}$	Saturation value
$_v$	Vapor phase

In this context, Liquefied Natural Gas (LNG) becomes especially relevant, as natural gas may be stored by decreasing its temperature below its boiling point, approximately 111 K at standard atmospheric pressure. In this state, it is much denser and requires about 600 times less volume for storage. LNG enables profitable transportation by sea in LNG carriers or by road in trucks, eliminating the need for a costly gas network and, therefore, helping to diversify gas suppliers. Albeit its market is still immature, small scale storage of LNG has seen a rise and is projected to continue expanding in the coming years, as it may become a key commodity in different sectors, such as fuel for road transportation or to generate off-grid power (see [3]).

Due to the cryogenic conditions required for its storage, heat ingress to LNG tanks is an unavoidable problem. This turns to be a major drawback, as it results in the heating of the stored LNG, which vaporizes as it reaches its boiling point following the process known as boil-off. The boil-off in the tank also triggers the auto-refrigeration process, which keeps LNG cold as it boils. However, as tank pressure rises (self-pressurization), the boiling point of LNG also increases. Thus, if tank pressure is not relieved, LNG starts to heat up. In small-sized LNG storage, the most commonly used tanks are type C pressure vessels, which can be designed to operate at high pressure values. This allows to hold LNG in a quiescent state for several days but, inevitably, if LNG inside the tank is not used or reliquefied, the generated boil-off gas (BOG) has to be vented out to maintain an acceptable tank pressure, with the consequent economic losses and environmental impact, as methane is one of the main greenhouse effect gases.

To the best knowledge of the authors, even though there is a significant body of research performing CFD analyses of the boil-off process, there are not many studies specifically dealing with tank self-pressurization and temperature stratification in small and quiescent tanks. For LNG tankers, boil-off rate (BOR) can be estimated using empirical relations, as detailed in [4], where a mathematical expression relating tank LNG volume and heat ingress with the BOR was presented. This expression leads to reasonable estimations of BOG production during a ship voyage where pressure, tank volume and fluid properties are approximately constant. However, it fails to account for a number of phenomena that become much more relevant in smaller sized tanks, such as the effect that temperature and pressure build-up have on the boil-off rate.

Other approaches rely on using state equations to relate thermodynamic variables governing the behavior of the fluid phases within the tank. In [5], models using Lee-Kesler-Plocker and Benedict-Webb-Rubin state equations were employed to predict BOG production in a tank assuming that the vapor and liquid phase were under thermodynamic equilibrium. Heat ingress was supplied as data, and the models were used in different tanks with varying LNG volume and operating pressures.

In [6], a system of ODEs derived from global mass and enthalpy balances and the Soave-Redlich-Kwong (SRK) equation of state was proposed to model the boil-off phenomena, considering the different components of LNG. The model was able to predict the evolution of their concentrations separately. Consequently, the weathering process of LNG could be assessed, as its composition changes over time, with more volatile components like nitrogen boiling first. Moreover, in [7], a detailed study aiming to characterize LNG losses due to boil-off in all the steps of an LNG tanker voyage was performed, including the loading and unloading process of the tanks and the BOG generation during laden and ballast voyages, considering several parameters.

One drawback with models relying on ODEs to model BOG generation in storage

tanks is that they may not completely account for the characteristics of the LNG flow inside the tank, driven by natural convection. In particular, the flow structures may depend on heat ingress, tank geometry or liquid level. Moreover, heat ingress is usually modeled in a simplified manner. Frequently, thermal equilibrium inside the tank is also assumed. Nevertheless, the actual conditions within small storage tanks under self-pressurization can substantially deviate from it. Thermal stratification in the liquid tends to appear as a warm layer at the free surface develops due to buoyancy (see [8]). In [9], the effect of the thermal aspect ratio on thermal stratification and self-pressurization was experimentally investigated in a liquid nitrogen storage tank. Their measurements show significant vapor superheating as well as stratification inside the liquid phase, which are shown to be dependent on the filling level of the tank. Comparable findings were obtained in [10] for a similar LN_2 tank. In addition, a thermal diffusion model was proposed to predict the self-pressurization curves, accounting for thermal stratification.

To investigate the details of LNG flow inside tanks, PDE models that consider Navier-Stokes equations can be used, which are much more computationally expensive to solve numerically. Related to this kind of approach, in [11], the flow field inside a rectangular water tank subjected to lateral heating was visualized to study thermal stratification in cryogenic tanks. Then, the axisymmetric LH_2 flow in a cylindrical cavity considering only the liquid with no vaporization was solved. In [12], the flow inside a 2d cut of a membrane tank was solved, considering a two-phase flow. The boiling process was modeled using a mass transfer source term, assuming a constant saturation temperature.

In [13], a detailed study of natural convection in an LNG tank was presented, aiming to investigate how tank gradual pressurization influences BOG generation. The proposed model solves the flow only for the liquid phase, given that the vapor is assumed to be at the same temperature as the liquid-vapor interface. It was concluded that the BOG generation rate is reduced as both pressure and tank size rises. In [14], a two-phase lumped vapor CFD model was used to investigate self-pressurization in a LH_2 storage tank for different filling levels, obtaining favorable agreement with the experimental observations from [15].

In [16], the flow due to free convection in a liquefied hydrogen tank was studied numerically using a 2d axisymmetric model. Boil-off was modeled using an expression based on the difference between saturation temperature and the temperature at the free surface, which was considered constant. The obtained stratification profiles for the temperature were compared for different tank aspect ratios. In [17], stratification was studied for a water tank under large incoming heat flux, replicating the conditions and observations made by [18], including a de-stratification process. A similar boil-off model was used, accounting for heat loss in the liquid and considering a pressure-dependent saturation temperature. The proposed model was enhanced in [19], including the conjugate heat transfer problem among the solid wall of the tank and the fluid phases.

CFD simulations were also used in [20] to investigate the diffusion and composition changes of leaked LNG through the insulation box of large storage tanks. In [21], a mixture model was used to study convection and self-pressurization in both a LN_2 and a LNG tanks, considering uniform heat flux values at the inner surface wall and different filling levels. Their results also show how thermal stratification is developed in the early stages of the considered cases. Moreover, in [22], a CFD simulation of a full-scale storage tank was presented, assessing BOG generation and flow dynamics. An estimation of the wall superheat needed for the inception of nucleate boiling was obtained, finding that it

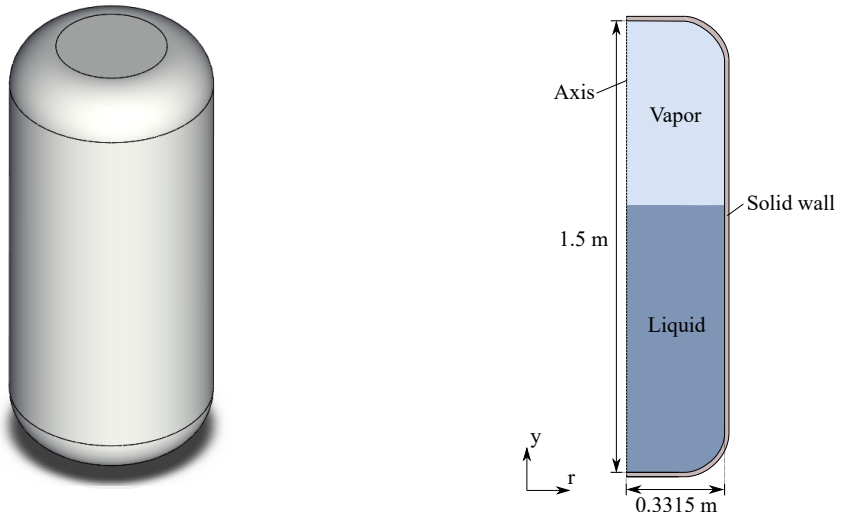

(a) 3d view.

(b) Schematic of a cross section of the tank.

Figure 1: Tank geometry.

is around 2.5-2.8 K.

At the present work, we aim to study the effect of pressurization in the boil-off process for a simplified prototype of a small-sized LNG storage tank using a CFD multiphase model. Different filling levels of the tank are considered, as well as the conjugate heat transfer problem involving the tank solid wall. Realistic data for material properties are used. The influence of the insulation layer thickness on heat ingress and flow structures is also investigated. In Section 2, we describe the physical problem, starting with the tank geometry. Then, the considered values for material properties and the complete mathematical model are presented. In Section 3, the numerical schemes, the computational grid and the procedure that are used to obtain the solution are described. In Section 4, the obtained results are discussed, both for varying filling levels and different insulation thickness values. Finally, in Section 5, some concluding remarks are addressed.

2. Mathematical model and problem statement

2.1. Problem description

A 0.5 m^3 cylindrical LNG storage tank is considered, depicted in Figure 1a. The inner chamber, which holds the fluids, has a height of 1.5 m and a maximum interior radius of 0.3315 m, as shown in Figure 1b. It is assumed to be fixed to the ground and completely quiescent. Thus, any fluid movement is triggered by heat ingress to the tank, which is responsible for both free convection and boil-off. The tank solid wall is composed of a w mm-thick evacuated perlite insulation layer and two 304 stainless steel vessels, each of them 3 mm-thick. In Figure 2, a schematic diagram with the different solid layers is displayed. For the filling level influence studies presented in Section 4.1, the considered value for the insulation thickness parameter is $w = 11$ mm. In Section 4.2, the influence of this parameter in the obtained results is investigated.

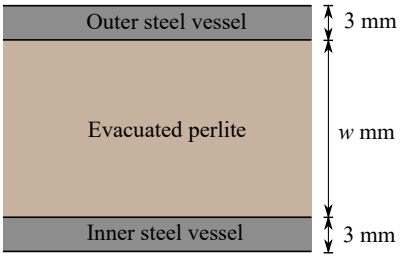

Figure 2: Layers inside the solid wall.

Given that the tank has a cylindrical structure, we assume that the flow also preserves this symmetry. Therefore, an axisymmetric problem is considered, such that the model is solved only in a 2d cut of the tank, as shown in Figure 1b. The tank is considered to be initially filled with LNG at constant temperature $T = 113$ K. Provided that the corresponding saturation pressure for this temperature is 1.13 bar, we choose this value as the initial pressure in the vapor phase.

2.2. Material properties

The composition of the LNG is assumed to be pure methane, which is a frequent assumption in similar studies, such as [13] or [22]. Given that LNG has a content of methane that is typically over 90%, its overall physical properties are very similar to those of liquefied methane. Consequently, the assumption of pure methane instead of a more realistic composition does not significantly change the flow structures, temperature stratification profiles or heat ingress to the tank. Nonetheless, it is worth mentioning that there is a number of shortcomings derived from this simplifying assumption. Namely, rollover and LNG weathering phenomena cannot be predicted by the model, as they are related to the multicomponent nature of LNG. For more details on rollover, we refer to [23]. In addition, the boil-off rate can be substantially different for a more realistic LNG composition. This is particularly relevant when a significant amount of nitrogen is present in the mixture, as it is a more volatile fluid than methane (see [6] or [7]).

At the liquid phase inside the tank, temperature variations are small. Thus, constant values for its properties are considered, as shown in Table 1. We use data corresponding to saturated liquid methane at 113 K, extracted from the National Institute of Standards and Technology (NIST) database, available in [24]. With ρ, k, c_p and μ, we denote density, thermal conductivity, specific heat and dynamic viscosity, respectively. Note that although density may be considered constant, buoyancy forces must still be included in order to account for free convection in the liquid phase. For this purpose, we use the Boussinesq approximation. Hence, the body force at the liquid $\mathbf{b}_l$ is represented by:

$$\mathbf{b}_l = \rho_l(1 - \beta(T - T_{Rb}))\mathbf{g}, \tag{1}$$

where $\beta = 3.54e-3$ K^{-1} denotes the thermal expansion coefficient and T_{Rb} is the reference temperature used for the approximation, which we consider equal to the initial temperature $T_0 = 113$ K. In addition, $\mathbf{g}$ is the gravitational acceleration vector.

Both latent heat of vaporization H_{vap} and saturation temperature T_{sat} are taken to be functions of pressure using the following expressions:

$$T_{sat}(p) = 65.3180 + 2.3371p^{0.2592}, \tag{2}$$

$$H_{vap}(p) = 5.4465e5 - 36.5741p^{0.5919}, \tag{3}$$

which have been obtained fitting the data available in [24] for liquid methane.

At the vapor phase, the specific heat is considered constant with value $c_{p,v} = 2230$ J/(kg·K). Moreover, as a significant degree of superheating may be reached, large temperature variations can occur. Thus, thermal conductivity and dynamic viscosity are considered as linear functions of the temperature fitting the data available in [24]:

$$\mu_v(T) = 3.610e - 8T + 5.639e - 7, \tag{4}$$

$$k_v(T) = 1.208e - 4T - 1.775e - 3. \tag{5}$$

Provided that one of the main interests of this work is to study the impact of tank self-pressurization on boil-off rate, density at the vapor phase is considered as a dependent variable of temperature and pressure using the Peng-Robinson equation of state:

$$p = \frac{RT}{V_m - b} - \frac{a\alpha}{V_m^2 - 2bV_m - b^2}, \tag{6}$$

where

$$a = \frac{0.45724R^2T_c^2}{p_c}, \quad b = \frac{0.7780RT_c}{p_c}, \quad \alpha = \left(1 + \kappa\left(1 - \left(\frac{T}{T_c}\right)^{0.5}\right)\right)^2, \tag{7}$$

$$\kappa = 0.37464 + 1.54226\omega_{ac} - 0.26992\omega_{ac}^2. \tag{8}$$

Values with c subindices are the critical properties of the fluid, i.e., the pressure, temperature and density at the critical point. Moreover, $\omega_{ac} = 0.0114$ is the accentric factor whereas V_m is the molar volume in m^3/mol and R is the ideal gas constant. The choice of the Peng-Robinson equation of state over a more traditional expression as the ideal gas law is motivated by the fact that the latter yields a worse approximation of the pressure values for the cryogenic temperatures inside the tank.

Insulating properties of evacuated perlite are heavily dependent on temperature values. Thus, to model heat transfer inside the solid wall of the storage tank, perlite thermal conductivity is considered as a function of temperature using the following expression, gathered from [25]:

$$k_p(T) = 1.911e - 4 + 3.476e - 12T^{3.6783}. \tag{9}$$

Both vessels of steel are built with the same material. However, the outer one, which is exposed to the environment, is approximately at ambient temperature (293 K). In contrast, the inner vessel is roughly at the temperature of the fluids in the tank, around 113 K. Therefore, we consider constant properties for the 304 stainless steel corresponding to those temperatures for the different vessels, using the data available in [26], as shown in Table 1. In addition, the used values and functions for the fluids and perlite are summarized. Note that the vapor density is computed using the equation of state (6).

	ρ [kg/m^3]	k [W/(m·K)]	c_p [J/(kg·K)]	μ [Pa·s]
Liquid phase	420.40	$1.82e-1$	3490	$1.13e-4$
Vapor phase	-	$k_v(T)$	2230	$\mu_v(T)$
Perlite	50	$k_p(T)$	837	-
Steel, inner vessel	8030	9.8	304.7	-
Steel, outer vessel	8030	15.1	470.5	-

Table 1: Physical properties for the liquid, the vapor and the solid materials. Source: [24, 26, 27].

2.3. Turbulence model

To assess if turbulence is of relevance in the flow, a dimensional analysis may be performed. A characteristic length defined as the liquid volume divided by the wall surface in contact with the liquid is considered ($L = 0.15$ m). This choice is motivated by the work [28], where numerical studies that analyzed a cylindrical cavity subjected to natural convection for varying Rayleigh numbers were conducted. For an estimated heat flux of $q = 20$ W/m^2, the Grashof number is equal to $2.67e10$ and the Rayleigh number is $5.79e10$. According to the criteria developed in [28], these numbers are indicative of a turbulent regime. Thus, in order to model the turbulent flow, we use the SST $K-\omega$ RANS turbulence model (see [29]), which uses a combination between the $K-\varepsilon$ in the free stream and a $K-\omega$ near the boundary layers. This allows to retain the good behavior of the $K-\omega$ model close to the walls, which is reported to perform better than $K-\varepsilon$ models in wall-bounded flows, as it can be extended to fully resolve the boundary layer without the use of damping functions (see [30]). This is a desirable feature to accurately model the heat transfer at the walls of the tank. The details concerning these models are extensively covered in the literature (see, for instance, [31] or [32]).

2.4. Multiphase flow

The flow in the tank is a two phase flow, with two distinct and immiscible phases separated by a free surface. To model these different phases, the Volume of Fluid method (VOF) is used, which is a front-capturing method proposed originally in [33] to solve free surface flows where a single fluid domain with fixed boundaries is considered. The computational domain is split in a fluid subdomain Ω_f and the solid wall Ω_s. Then, the fluid subdomain can be decomposed as $\Omega_f = \Omega_l(t) \cup \Omega_v(t) \cup \Gamma_{int}(t)$, where $\Omega_l(t)$ is the liquid phase subdomain, $\Omega_v(t)$ is the vapor phase subdomain and $\Gamma_{int}(t)$ is the free surface between both phases, which all depend on time t. A piecewise constant function ξ_l that is discontinuous at $\Gamma_{int}(t)$ is used to track the free surface position:

$$\xi_l(\mathbf{x}, t) = \begin{cases} 1, & \mathbf{x} \in \Omega_l(t), \\ 0, & \mathbf{x} \notin \Omega_l(t). \end{cases} \tag{10}$$

This function is numerically approximated using the so-called volume fraction α_l, which takes a constant value at each cell in the grid. The value of α_l is interpreted as the fraction of it occupied by the liquid phase. Then, the vapor phase volume fraction is readily obtained, as it must satisfy that $\alpha_v = 1 - \alpha_l$. Values other than 0 or 1 for the volume fraction represent a mixture of the fluid phases and indicate that the free surface is located inside the corresponding cell.

With the VOF method, only one set of conservation equations is solved for both fluid phases, using mixture properties. For an arbitrary property field ϕ it is considered that

$$\hat{\phi} = \alpha_l \phi_l + \alpha_v \phi_v = \alpha_l \phi_l + (1 - \alpha_l)\phi_v, \tag{11}$$

where ϕ_l and ϕ_v denote the values corresponding to the liquid and vapor phases, respectively.

Therefore, all relevant fluid properties, such as density ρ, viscosity μ, specific heat c_p or thermal conductivity k, are considered as mixture properties when solving the conservation equations. To ensure the accuracy of the method, the cells containing the vapor-liquid free surface should be sufficiently small.

2.5. Boil-off model

To model the boiling process of the liquid phase, appropriate source terms are added to the conservation equations. We use an analogous model to the one described in [16, 17, 21, 22], known as *Lee model*. It uses the following source term to model mass transfer from the liquid to the vapor:

$$\dot{m}_{lv} = \begin{cases} \gamma \alpha_l \rho_l \dfrac{T - T_{sat}(p)}{T_{sat}(p)}, & \text{if } T > T_{sat}(p), \\ \\ \gamma \alpha_v \rho_v \dfrac{T - T_{sat}(p)}{T_{sat}(p)}, & \text{if } T \leq T_{sat}(p), \end{cases} \tag{12}$$

where γ is a coefficient related to the vaporization rate, with units s^{-1}. The saturation temperature T_{sat} is obtained as a function of pressure, using (2). According to expression (12), temperature values below the saturation one result in condensation of the vapor whereas temperature values above saturation lead to the vaporization of the liquid. In the proposed case, heat ingress to the tank causes a temperature rise, which triggers the vaporization process. Condensation is negligible, unless the pressure rises rapidly, which can occur in real conditions when the available volume for vapor reduces significantly due to thermal expansion of the liquid. In our computations, the term due to condensation in (12) is not included in the model.

The expected heat flux to the tank is around 20 $\mathrm{W/m^2}$. This heat flux value is well below the required amount to produce nucleate boiling in the liquid phase. Thus, the phase change should take place at the free surface separating the fluid phases. Consequently, the source term (12) is only applied in computational cells where the free surface is present, this is, those cells satisfying that $\alpha_l \neq 1$ and $\alpha_l \neq 0$.

The latent heat of vaporization is absorbed as the liquid evaporates. To model this phenomenon, we introduce the following source term in the energy conservation equation:

$$S = -H_{vap}(p)\dot{m}_{lv}. \tag{13}$$

2.6. Governing equations

The flow inside the tank is modeled using the unsteady Reynolds-Averaged Navier-Stokes equations, with the VOF method to account for the multiphase flow. As described in Section 2.4, this implies that mixture properties are used and that only one set of

conservation equations is solved. The previously detailed source terms are incorporated to model the phase change, as well as the equations for the turbulence model variables.

The mass conservation equation is given by:

$$\frac{\partial \hat{\rho}}{\partial t} + \mathrm{div}(\hat{\rho}\mathbf{v}) = 0, \tag{14}$$

where $\mathbf{v}$ denotes the mean velocity field.

An advection equation for the liquid volume fraction α_l is also solved:

$$\frac{\partial(\alpha_l \rho_l)}{\partial t} + \mathrm{div}(\alpha_l \rho_l \mathbf{v}) = -\dot{m}_{lv}, \tag{15}$$

where the term $\dot{m}_{lv}$ is obtained using expression (12) and governs the boil-off process. Provided that $\alpha_l + \alpha_v = 1$, there is no need to solve an equation for the volume fraction of the vapor phase.

In addition, the momentum conservation equation is solved to obtain the mean velocity field, which is shared among the fluid phases:

$$\begin{aligned}\frac{\partial(\hat{\rho}\mathbf{v})}{\partial t} + \mathrm{div}(\hat{\rho}\mathbf{v}\otimes\mathbf{v}) = &-\mathrm{grad}\ p - (\rho_l \alpha_l (1-\beta(T-T_{Rb})) + \rho_v(1-\alpha_l))\,\mathbf{g} \\ &+ \mathrm{div}\left((\hat{\mu}+\hat{\mu}_T)\left[\mathrm{grad}\ \mathbf{v} + \mathrm{grad}\ \mathbf{v}^t - \frac{2}{3}(\mathrm{div}(\mathbf{v}))\mathbf{I}\right] - \frac{2}{3}\hat{\rho}K\mathbf{I}\right),\end{aligned} \tag{16}$$

where the turbulent viscosity μ_T is obtained from the turbulence model variables K and ω (see [32]).

To find the temperature in the fluids, the energy conservation equation is solved:

$$\frac{\partial(\hat{\rho}E)}{\partial t} + \mathrm{div}(\mathbf{v}(\hat{\rho}E + p)) = \mathrm{div}((\hat{k} + \hat{k}_T)\mathrm{grad}\ T) + S, \tag{17}$$

where k_T is the turbulent thermal conductivity, computed using the turbulent viscosity (see [32]). E denotes the mass-averaged total specific energy, which is defined as:

$$E = \frac{\alpha_l \rho_l E_l + \alpha_v \rho_v E_v}{\alpha_l \rho_l + \alpha_v \rho_v}, \tag{18}$$

where the liquid and vapor energy E_l and E_v are computed from

$$E_l = \int_{T_{\mathrm{ref}}}^{T} c_{p,l}(s)ds + \frac{\mathbf{v}^2}{2}, \tag{19}$$

$$E_v = \int_{T_{\mathrm{ref}}}^{T} c_{p,v}(s)ds - \frac{p}{\rho_v} + \frac{\mathbf{v}^2}{2}. \tag{20}$$

The liquid phase is considered incompressible whereas the vapor is compressible. Pressure, density and temperature for the vapor phase have to satisfy the Peng-Robinson equation of state (6).

Lastly, conservation equations for the turbulent kinetic energy K and specific dissipation rate ω are solved:

$$\frac{\partial(\hat{\rho}K)}{\partial t} + \mathrm{div}(\hat{\rho}K\mathbf{v}) = \mathrm{div}\left[\left(\hat{\mu} + \frac{\hat{\mu}_T}{\sigma_K}\right)\mathrm{grad}\ K\right] + G_K - Y_K, \tag{21}$$

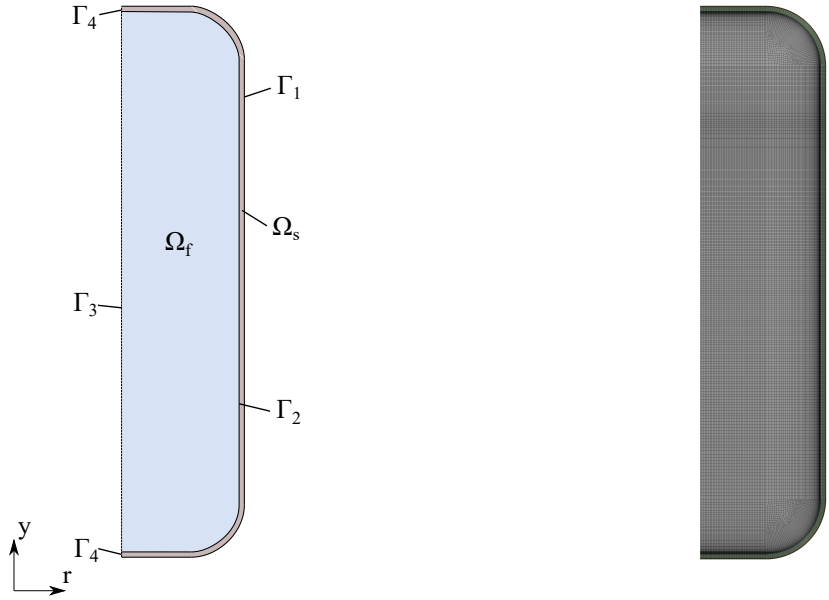

(a) Boundaries and subdomains. (b) Grid.

Figure 3: Computational domain and grid.

$$\frac{\partial(\hat{\rho}\omega)}{\partial t} + \operatorname{div}(\hat{\rho}\omega\mathbf{v}) = \operatorname{div}\left[\left(\hat{\mu} + \frac{\hat{\mu}_T}{\sigma_\omega}\right)\operatorname{grad}\,\omega\right] + G_\omega - Y_\omega + D_\omega. \tag{22}$$

For the sake of brevity, we omit the details of the turbulent constants, the K and ω production terms G_K and G_ω, the dissipation terms Y_K and Y_ω and the cross-diffusion term D_ω. For the precise details on their definition for the SST $K-\omega$ turbulence model, see [32]. In the solid subdomain Ω_s, the heat equation is solved:

$$\rho c_p \frac{\partial T}{\partial t} + \operatorname{div}(k\,\operatorname{grad}\,T) = 0. \tag{23}$$

We remark that the model that we solve is a 2d axisymmetric one. Therefore, equations (14)-(17) and (21)-(23) are rewritten in cylindrical coordinates assuming that the derivatives in the azimuthal direction vanish.

2.7. Boundary and initial conditions

The boundary of the storage tank is decomposed as depicted in Figure 3a. On the exterior boundary Γ_1, we impose that there is convective heat exchange with the air surrounding the tank:

$$-k\frac{\partial T}{\partial \mathbf{n}} = h(T - T_{\text{ext}}), \tag{24}$$

where the value of the external temperature is $T_{\text{ext}} = 293$ K and the heat transfer coefficient is $h = 7\ \text{W}/(\text{m}^2 \cdot \text{K})$.

Filling level	10%	20%	40%	60%	80%
y_0 [m]	0.16	0.31	0.60	0.90	1.19
A_l [m^2]	0.55	0.91	1.51	2.14	2.74
m_l [kg]	19.27	41.04	83.13	126.67	168.76

Table 2: Initial height of the free surface (y_0), wall surface area in contact with the liquid (A_l) and initial mass of liquid (m_l) for the considered filling levels.

On Γ_2, which corresponds to the interface between the solid and fluid subdomain, i.e., the inner wall of the tank, we set a no-slip condition ($\mathbf{v} = \mathbf{0}$). Moreover, continuity of heat flux and temperature has to be satisfied.

On the symmetry axis, which corresponds to $\Gamma_3 \cup \Gamma_4$, an axis boundary condition is applied, which implies that the normal derivatives of all involved variables are zero.

Suitable initial conditions have to be considered. In Ω_f, we assume that both phases are initially quiescent, i.e., that their velocity is zero. Moreover, a constant initial temperature of 113 K is set and the initial vapor pressure is 1.13 bar. This pressure is an operating pressure, which is used only for the computations related to the equation of state and not for the solution of the actual PDEs. This value is updated at each time step as tank pressure rises. Additionally, α_l values are set according to the filling level in the tank following the values presented in Table 2, where the wall surface area in contact with the liquid and the initial mass of liquid are also gathered. Lastly, initial conditions for the turbulent variables K and ω are also supplied. We assume that $K = 0$ m^2/s^2 and $\omega = 1$ s^{-1}.

In the solid subdomain Ω_s, corresponding to the perlite insulation and the two steel vessels, we consider a temperature profile $T_{0,s}$ as initial condition. This profile is the solution of the steady-state heat equation in Ω_s with boundary conditions $T = 113$ K on Γ_2 and the convective-type boundary condition given by expression (24) on Γ_1.

3. Numerical simulation

3.1. Discretization

The commercial software ANSYS Fluent 19.0 is used to solve the proposed model, which uses a cell-centered finite volume method to solve the equations. Coupling among velocity and pressure is done using the SIMPLEC iterative algorithm. Diffusive terms are discretized using least squares cell-based schemes. Moreover, QUICK schemes are used for the convective terms. In order to interpolate pressure values at the cell faces, the PRESTO! scheme is used. Time discretization is done using a First Order Implicit scheme and the Geo Reconstruct scheme is considered for the volume fraction equation, which is crucial to reduce numerical diffusion at the interface among the liquid and vapor phases. For more details about these numerical schemes, we refer to [32] or [34].

3.2. Solution procedure

To obtain the numerical solution of the problem, a smaller time step is selected at the start in order to help stability and convergence. We recall that the initial condition in the solid subdomain Ω_s is set as the solution of a steady state problem solved only in this subdomain. Therefore, we proceed as follows:

	No. of cells	Mean size (m)
Grid 1	3204	$1.27e-2$
Grid 2	12676	$6.40e-3$
Grid 3	45806	$3.37e-3$
Grid 4	163488	$1.78e-3$

Table 3: Computational grids chosen for the grid sensitivity study.

- *Steady-state problem.* To find the profile $T_{0,s}$, corresponding to the initial temperature at the solid wall Ω_s, fixed temperature conditions $T = 113$ K are imposed on the solid-fluid interface Γ_2. The steady state heat equation is then solved only at Ω_s.

- *Transient problem.* The model described in Section 2.6 is solved in Ω_f and Ω_s as follows:

  - 20 time steps are solved with $\Delta t = 0.001$ s, using the previously computed temperature profile in Ω_s and the values described in Section 2.7 in Ω_f.
  - A constant time step of $\Delta t = 0.01$ s is used until the end time t_{end} is reached.

The time step size is heavily restricted in order to comply with the Courant number stability criterion. Although velocities are low, the small-sized cells near the vapor-liquid interface and the inner wall of the tank lead to short time-step size requirements. This turns out to be the main bottleneck in the solution of this model, as it takes a very large number of time steps to reach sufficiently large time values to draw conclusions concerning the behavior of the tank.

3.3. Grid validation

To solve the model, a computational grid of the domain Ω was constructed. The grid is refined at the zones where large gradients are expected, which are the boundary layer at the solid wall and the area close to the starting position of the free surface between liquid and vapor. The dimensionless distance to the wall (y^+) of the cell centroids next to it is adjusted to achieve $y^+ \sim 1$ and ensure that it is inside the viscous sublayer, avoiding the usage of wall functions.

A grid sensitivity study was performed for the grid sizes reported in Table 3. All grids are constructed in an analogous manner and have approximately the same y^+ values for the near-wall cells. In Figure 3b, Grid 3 is shown.

The study consists in solving the proposed model with the tank filled up to an 80% level for $w = 11$ mm until reaching a time value $t_{\text{end}} = 3$ h. At this time value, in Figure 4a, we compare the velocity magnitude at the vertical wall boundary layer at a height $y = 0.75$ m. In Figure 4b, the temperature profile along the tank symmetry axis is displayed for the liquid phase. All grids show similar results, although Grids 1 and 2 result in slightly different temperature values near the free surface. In Figure 5a, the boil-off rate over time is depicted, whereas Figure 5b shows the pressure over time. Grid 1 and Grid 2 produce somewhat different results when compared to the finest grid sizes. Thus, we conclude that Grid 3 is sufficiently fine to solve the problem and is used to obtain the subsequently presented results.

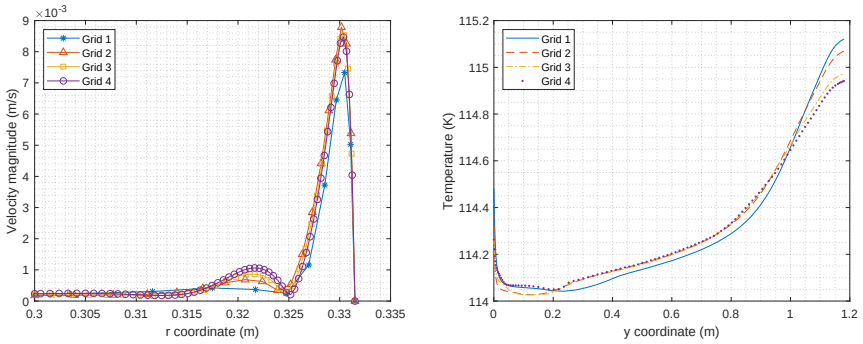

(a) Velocity magnitude. (b) Temperature.

Figure 4: Solution values for the considered computational grids at time $t = 3$ h.

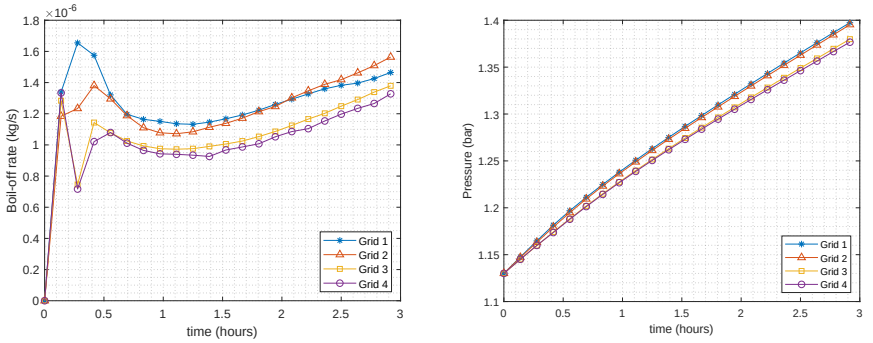

(a) Boil-off rate. (b) Pressure.

Figure 5: Boil-off rate and pressure for the considered computational grids.

3.4. Sensitivity study on parameter γ

One shortcoming of the boil-off model described in Section 2.5 is that it relies on the tuning of the parameter γ. Ideally, a value that matches experimental measurements should be used. When not possible, it is recommended to take values that keep the interface temperature close to the saturation temperature (see [35]). Different values have been reported for this coefficient in the literature. In [22], a value of 0.1 was used, whereas in [17] a value of 1 was chosen. Much higher values, reaching $\gamma = 100$, have been used in numerical simulation of boiling in microchannels (see [36]). Moreover, in [22], it was reported that the variation of the value of this parameter produced negligible effects in the computed evaporation rate in a full-scale LNG storage tank.

For the presented set-up, assuming an 80% filling level and considering Mesh 3, we compare the results for γ values ranging from 0.01 to 1. The obtained boil-off rates for different γ values after 5 h of simulation are shown in Table 4, whereas in Figures 6a and 6b the boil-off rate and pressure are depicted over time. Even if the influence of the parameter seems non-negligible, the boil-off rate is within 16% difference for γ values differing by a factor of two orders of magnitude. In addition, the difference is particularly relevant at the start of the simulation and slightly reduces over time. For longer time

values, the boil-off rates would be more similar. The vapor pressure is very similar for the tested γ values. Consequently, we use the value $\gamma = 0.1$ for all the reported numerical simulations.

In all the boil-off rate over time depictions in this work, such as Figure 6a, the maximum BOR is reached at the very initial times, with a value of around $3e-6$ kg/s for $\gamma = 0.1$. This is hidden by the time scale of the points used to construct the graphs. The value is highly dependent on the γ parameter choice and it is a non-physical artifact of the model, as the phase equilibrium at a uniform $T = 113$ K temperature with an initial zero boil-off rate is not a realistic starting point for the computations. Thus, boil-off rate rises quickly at the beginning of the computations as the warm liquid reaches the free surface and stabilizes at a lower value immediately afterwards. This has little influence in the vapor mass values, as shown in Figure 6c, given that the time interval

γ	BOR [kg/s]	p [bar]
1	$2.21e-6$	1.58
0.1	$1.97e-6$	1.54
0.01	$1.90e-6$	1.52

Table 4: Computed boil-off rate and pressure at $t = 5$ h for different γ values.

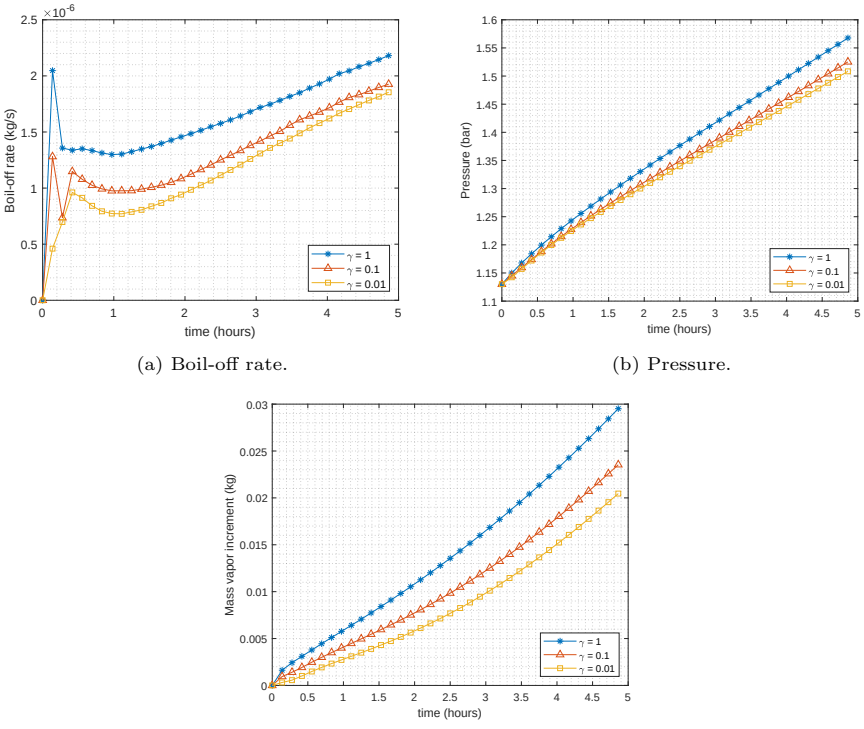

(a) Boil-off rate.

(b) Pressure.

(c) Vapor mass increment.

Figure 6: Influence of the γ parameter.

during which this behavior is exhibited is short.

4. Results

The mathematical model described in Section 2 is solved until reaching $t_{\text{end}} = 5$ h using the software ANSYS Fluent 19.0. This end time value was considered enough to investigate the flow structures arising from natural convection inside the tank and to show the main trends of the behavior of the tank. The procedure detailed in Section 3 is followed for all the considered cases to solve the model. The simulations are run using 16 cores at a computer cluster composed of 25 Dell PowerEdge machines, ranging from R815 ones, equipped with AMD Opteron 6174 processors, to C6220 II systems with Intel Xeon E5-2637 v4 processors. Convergence is achieved at each time step if the globally scaled residuals for all variables are below $1e-6$.

4.1. Filling level influence study

The filling levels reported in Table 2 are considered as initial condition for the model. In Figure 7, contours of the stream function are displayed for various time values for the 80% filling level.

As shown in Figure 7a, the warm liquid rises along the side wall of the tank due to the buoyancy force and turns towards the tank axis after reaching the free surface. Then, it moves downward forming the primary circulation in the tank. A secondary circulation is developed near the free surface as time advances, as shown in Figure 7b. More complex and transient flow structures are generated in the bottom of the tank due to the heat leak coming from the bottom wall. Since the difference between stream function values at each time snapshot represents the mass flow rate between the streamlines that they define, it is observed that the primary circulation in the flow is more vigorous at the early stages and weakens over time.

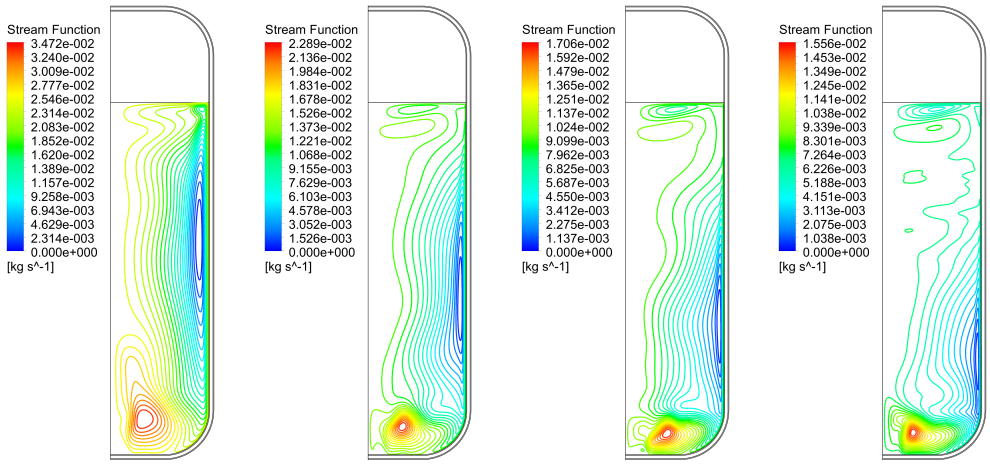

(a) $t = 15$ min. (b) $t = 1$ h. (c) $t = 2$ h. (d) $t = 5$ h.

Figure 7: Stream function contours, 80% filling level.

Analogous results are obtained for the 60% and 40% filling levels, as depicted in Figure 8, where the stream function contours are shown for the 40% level, evidencing similar flow circulations. However, for the lower filling levels the results differ substantially, especially for the 10% level. At these levels, the circulations generated at the bottom of the tank now affect the whole bulk of the liquid, as shown in Figure 9, where the streamlines for the 10% level are displayed.

In all the considered cases, the highest velocity values are obtained in the boundary layer next to the tank inner wall in both in the vapor and the liquid. In Figure 10, the contours of velocity magnitude are displayed at $t = 5$ h for various filling levels. The

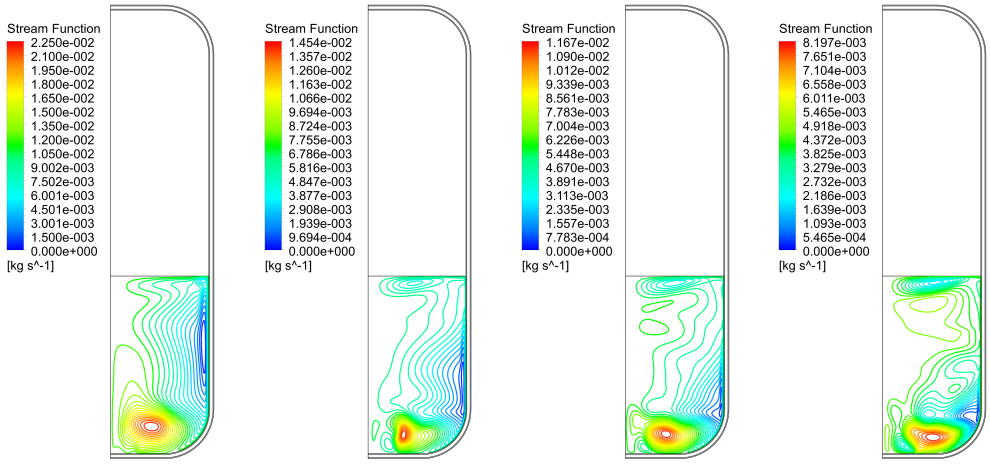

(a) $t = 15$ min. (b) $t = 1$ h. (c) $t = 2$ h. (d) $t = 5$ h.

Figure 8: Stream function contours, 40% filling level.

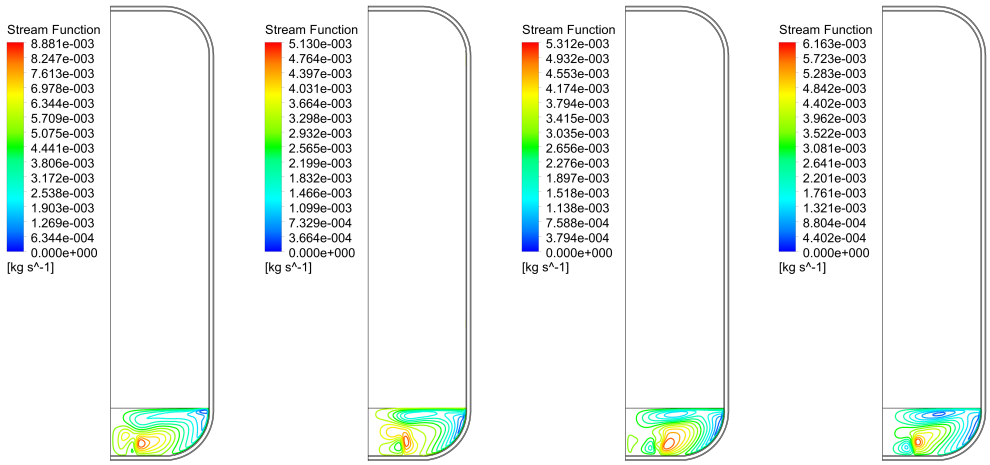

(a) $t = 15$ min. (b) $t = 1$ h. (c) $t = 2$ h. (d) $t = 5$ h.

Figure 9: Stream function contours, 10% filling level.

scale hides the value of bulk fluid motion, as it is comparatively smaller than that in the boundary layer. Velocities are also significantly large at the generated circulations in the bottom of the tank and upon reaching the free surface.

As time advances, heat ingress results in an increase of the internal energy in both phases and, consequently, tank pressure rises. Even though the initial temperature inside the tank is homogeneous, the temperature profiles along the vertical coordinate show early stratification in both phases. This is depicted for the different filling levels and the time values $t = 2$ h and $t = 5$ h in Figures 11 and 12 along the symmetry axis of the storage tank. To compare the results in the liquid phase, the vertical coordinate y is presented as a dimensionless height y/y_0, where y_0 is the height of the free surface, which varies for each filling level. As the boil-off rates are low in all cases, the free surface barely moves from the initial position. Thus, the values gathered in Table 2 are used as y_0. In the vapor phase, the dimensionless height is defined as $(y - y_0)/(L - y_0)$, where

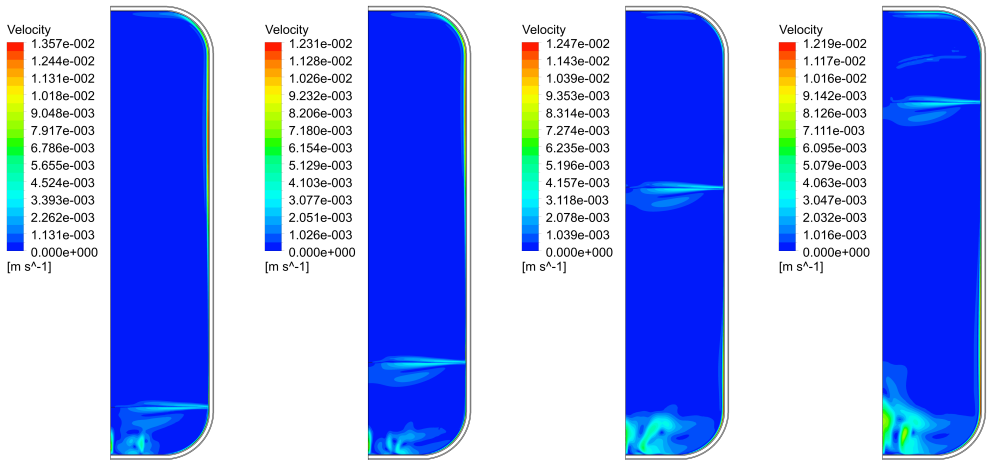

(a) 10% filling level. (b) 20% filling level. (c) 60% filling level. (d) 80% filling level.

Figure 10: Velocity magnitude contours, $t = 5$ h.

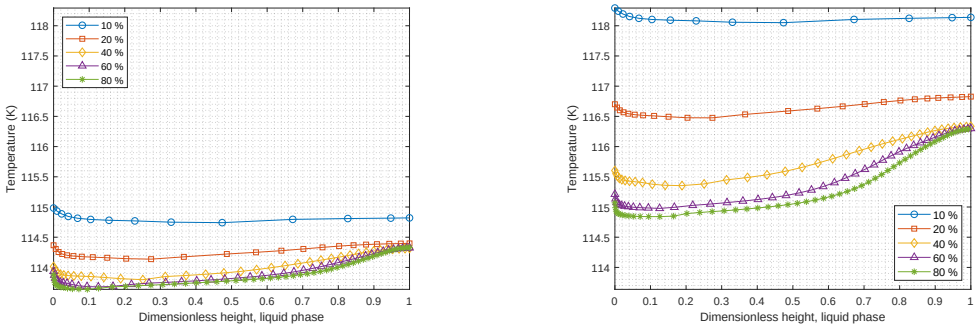

(a) $t = 2$ h. (b) $t = 5$ h.

Figure 11: Stratification at the liquid phase for different filling levels and time values.

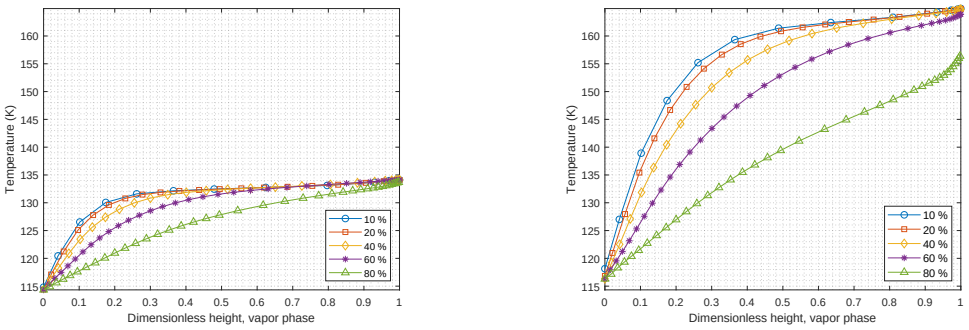

(a) $t = 2$ h. (b) $t = 5$ h.

Figure 12: Stratification at the vapor phase for the considered filling levels and time values.

$L = 1.5$ m is the total height of the inner vessel of the tank.

Both in the liquid and vapor phases the stratification degree grows as time advances and is especially relevant in the area closer to the free surface. In the liquid, stratification is highly dependent on the filling level of the tank. Significant stratification is observed in the 80%, 60% and 40% levels, with the bottom part of the tank being in a subcooled state. Nevertheless, for lower levels, stratification weakens substantially. In particular, at the 10% level, the liquid is essentially isothermal. The vapor phase displays significant superheating, following profiles with respect the dimensionless height that are very similar in all the considered filling levels. Slightly steeper temperature gradients close to the free surface are obtained in the lower filling levels.

The numerically found temperature stratification profiles are in qualitative agreement with experimental results reported for different set-ups in small cryogenic tanks. In [9] and [10], the measured temperature profiles in a liquid nitrogen tank also showed vapor superheating. At higher filling levels, the temperature in the free surface was larger than the bulk temperature as a consequence of a bigger stratification degree, with stratification increasing over time. Similar temperature profiles were measured in a liquid hydrogen tank in [15].

Total heat ingress to the tank over time for the considered filling levels is depicted in Figure 13b. For higher filling levels, the obtained heat ingress is larger. Experimental studies in cryogenic vessels, such as [37], have reported similar findings. However, a more detailed analysis of the average heat flux $\overline{q}_l$ per unit area, considering only the part of the wall in contact with the liquid phase, reveals larger values for the smaller filling levels, as displayed in Figure 13a. This is not in contradiction with the total heat ingress results, as the surface area in contact with the liquid is smaller for lower filling levels, as reported in Table 2. The larger heat flux values in these levels can be related to the flow structures, as liquid mixing becomes more efficient, especially at the 10% level.

Computed boil-off rates are shown over time for the different filling levels in Figure 13c. A decreasing-increasing trend with decreasing filling level is observed. In particular, a larger boil-off rate is computed at the 80% level when compared to the 60% and 40% levels, which is mainly due to the larger amount of liquid mass. This decreasing trend is not observed when considering the boil-off rate in %/day (see Table 5). For

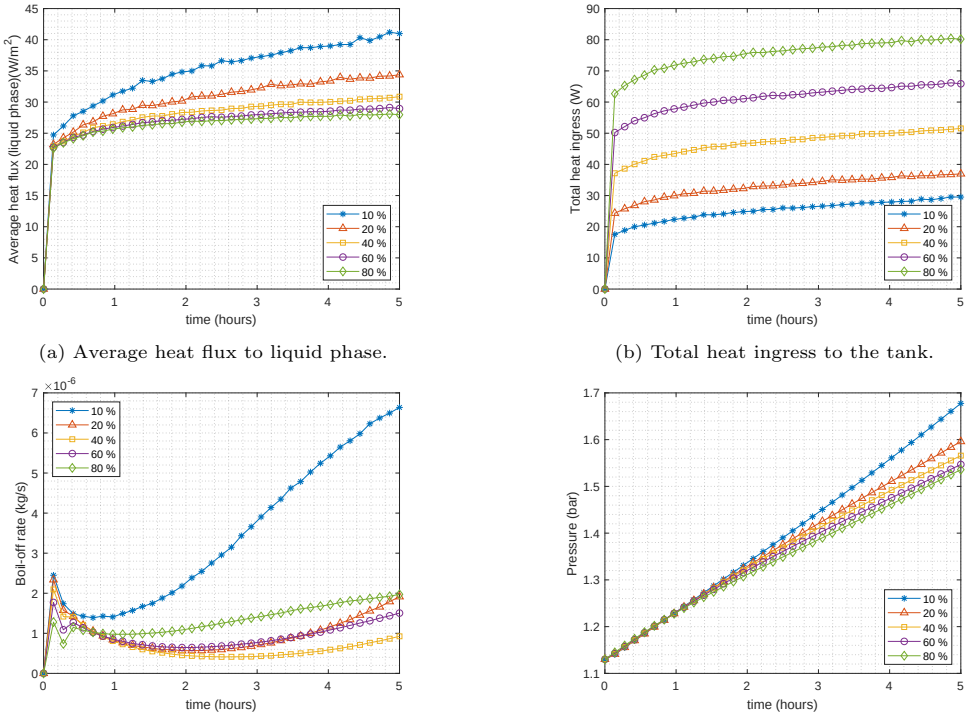

(a) Average heat flux to liquid phase.

(b) Total heat ingress to the tank.

(c) Boil-off rate.

(d) Vapor pressure.

Figure 13: Evolution over time of several variables depending on tank filling level.

the lower filling levels (10% and 20%), an increasing trend is observed, with the boil-off rate at the 10% becoming much higher than in the remaining levels. Due to the fast self-pressurization, most of the incoming energy is used to raise liquid temperature. Therefore, the high boil-off rate for the 10% may be partly explained by the especially worse heat ingress to liquid mass ratio (see Table 2), which is three times larger than in the 80% level. In addition, the enhanced liquid mixing may also play a role, resulting in larger average heat fluxes per unit area to the liquid phase, as discussed previously.

In Figure 13d, the vapor pressure values are depicted over time. In the considered time interval, the vapor pressure profiles are almost linear. Similar pressurization rates are obtained for all the considered levels, showing that for lower filling levels self-pressurization is faster. Similar results were computationally obtained in [14]. Nevertheless, our numerical results contrast with the experimental findings in [9], which report higher pressurization rates for larger filling levels. This suggests that an accurate representation of the pressurization rate at the larger filling levels might need to include the thermal expansion of the liquid, as the available volume for the vapor may be significantly reduced. Further studies should aim to address this effect.

In Table 5, we gather the boil-off rates, total heat flux and the average heat flux to the liquid phase for all the considered filling levels, computed at the end time $t = 5$ h.

	BOR [%/day]	BOR [kg/s]	Q [W]	$\overline{q}_l$ [W/m^2]
10%	$2.98e+0$	$6.64e-6$	29.52	40.99
20%	$4.03e-1$	$1.91e-6$	36.96	34.39
40%	$9.62e-2$	$9.26e-7$	51.55	30.87
60%	$1.03e-1$	$1.50e-6$	65.86	28.95
80%	$1.01e-1$	$1.97e-6$	80.20	27.97

Table 5: Boil-off rates, total heat flux, heat flux to the liquid phase and pressurization rate for the considered filling levels at $t = 5$ h.

The values are consequent with the prior discussion, showing that for the 10% filling level, the average heat flux to the liquid phase $\overline{q}_l$ is around 50% bigger. However, the total heat ingress to the tank Q is substantially lower.

4.2. Insulation layer thickness influence study

The described mathematical model can be used to investigate the influence of the insulation layer thickness in the flow. In particular, heat leak and boil-off in the tank can be also characterized, as well as the pressurization rate. With this purpose, the CAD slice of the tank, shown in Figure 1b, is slightly changed increasing or decreasing the evacuated perlite layer thickness w, which was previously equal to 11 mm. Then, the mathematical model is solved, assuming an 80% filling level. We consider the values $w = 5.5$ mm, $w = 8.25$ mm, $w = 16.5$ mm and $w = 22$ mm.

In Figure 14, the stream function contours for different insulation thicknesses are shown at $t = 5$ h. The flow structures are very similar to the previously described ones for $w = 11$ mm. However, the contour values indicate that the circulations in the tank become more vigorous as insulation thickness decreases. This is a consequence of the higher heat ingress to the tank, which grows for lower insulation thickness values, as

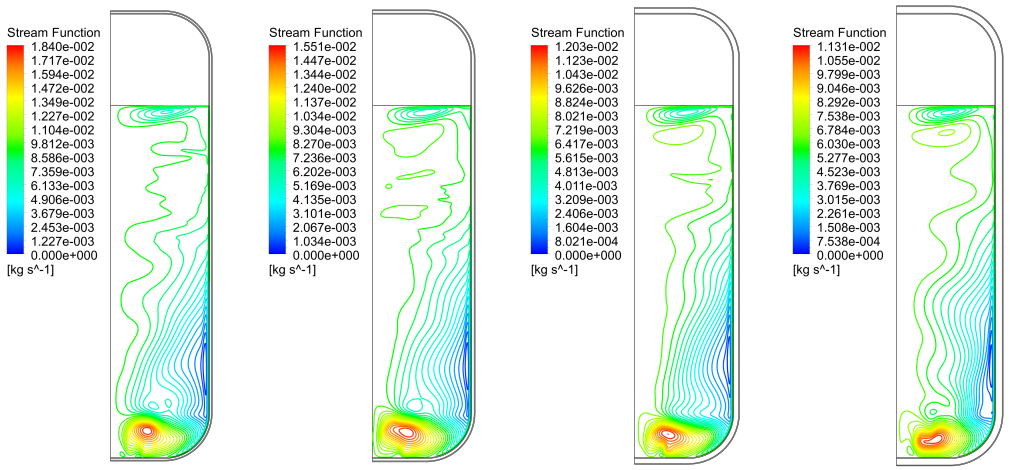

(a) $w = 5.5$ mm. (b) $w = 8.25$ mm. (c) $w = 16.5$ mm. (d) $w = 22$ mm.

Figure 14: Streamlines for 80% filling level at time $t = 5$ h and different insulation thickness values.

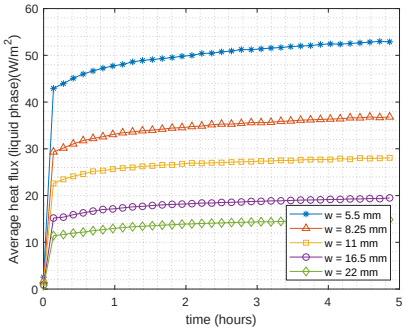

(a) Average heat flux to liquid phase.

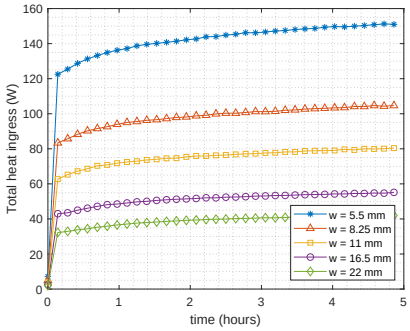

(b) Total heat ingress to the tank.

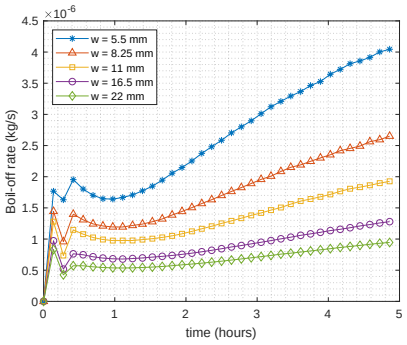

(c) Boil-off rate.

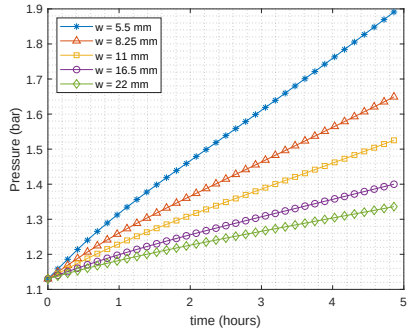

(d) Vapor pressure.

Figure 15: Evolution over time of several variables for different insulation layer thickness.

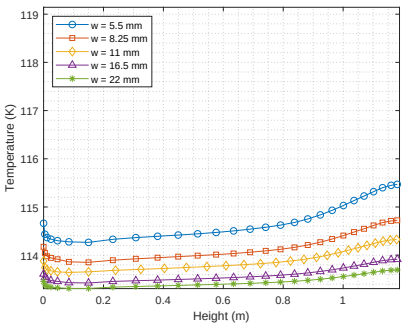

(a) $t = 2$ h.

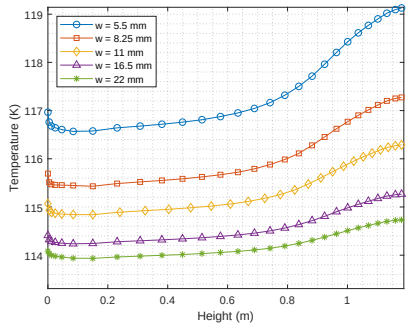

(b) $t = 5$ h.

Figure 16: Temperature stratification along the symmetry axis for 80% filling level at the liquid phase, considering different time and insulation layer thickness values.

500 displayed in Figure 15b, where the total heat ingress to the tank is shown over time for all the considered values of w. The average heat flux to the liquid phase through the tank inner wall is shown over time in Figure 15a, which is also larger as thickness decreases. Larger heat ingress to the tank leads to increased boil-off rates, as depicted in Figure

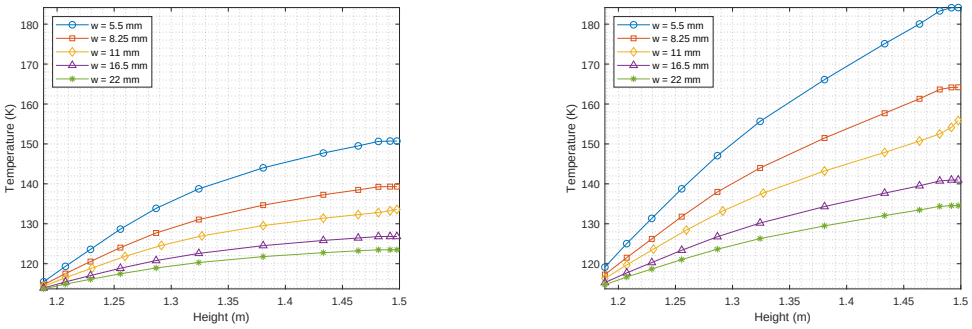

(a) $t = 2$ h. (b) $t = 5$ h.

Figure 17: Temperature stratification along the symmetry axis for 80% filling level at the vapor phase, considering different time and insulation layer thickness values.

15c. Pressurization rates behave similarly, increasing with bigger heat leak into the tank, as displayed in Figure 15d. This behavior was observed experimentally in [15], where higher pressurization rates were measured for increased heat ingress to the tank.

In Figures 16 and 17, the temperature values along the symmetry axis are compared for various insulation thicknesses and time values, both in the liquid and vapor phases. The results evidence that the stratification degree is increased as the heat ingress to the tank grows, resulting in larger temperature differences between the bottom of the tank and the free surface. In addition, larger heat ingress also results in faster superheating of the vapor. In Table 6, we gather the boil-off rates, total heat flux and average heat flux to the liquid for all the considered insulation thicknesses, computed at the final time $t = 5$ h.

The relation among the heat ingress and the insulation thickness is displayed in Figure 18a, where the obtained points are fitted using a function of the form $f(Q) = AQ^B$. The computed coefficients are $A = 736.7$ and $B = -0.9249$. Similar relations can be readily established among the insulation thickness and the boil-off rate, provided that the relation

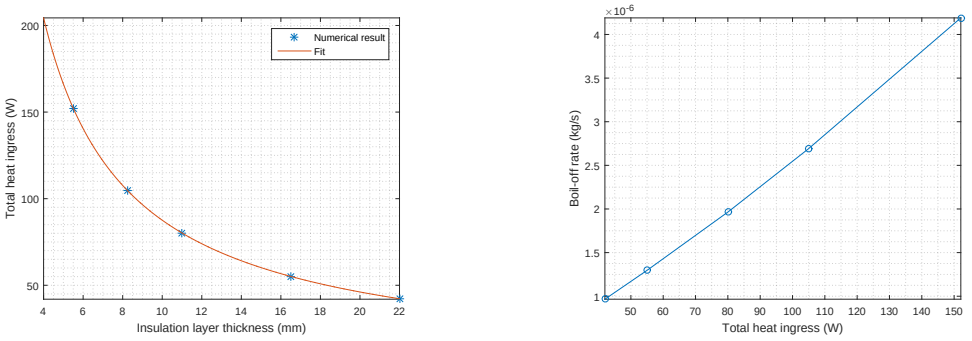

(a) Insulation layer thickness. (b) Boil-off rate.

Figure 18: Obtained insulation layer thickness and boil-off rate with respect to the total heat ingress.

w [mm]	BOR [%/day]	BOR [kg/s]	Q [W]	$\overline{q}_l$ [W/m^2]
5.5	$2.14e-1$	$4.19e-6$	152.07	53.27
8.25	$1.38e-1$	$2.69e-6$	104.94	36.92
11	$1.01e-1$	$1.97e-6$	80.20	27.97
16.5	$6.64e-2$	$1.30e-6$	55.13	19.49
22	$4.95e-2$	$9.66e-7$	41.96	14.85

Table 6: Boil-off rates, total heat flux and heat flux to the liquid phase for the considered insulation thickness values at time $t = 5$ h.

among the heat ingress and the boil-off rate is approximately linear, as shown in Figure 18b.

5. Conclusions

A systematic study of the flow and conjugate heat transfer inside a 0.5 m^3 LNG storage tank was presented using CFD. LNG was assumed to be composed of pure methane. Realistic values, extracted from the literature, were used for the properties of solid materials and fluid phases.

Temperature stratification, boil-off and self-pressurization were studied for various filling levels and insulation layer thicknesses of the tank, as well as the dynamic behavior of both the liquid and vapor phases. The temperature profiles in the liquid phase were shown to be depend on the filling level and the insulation layer thickness. For low filling levels, almost isothermal profiles were obtained in the liquid. The degree of thermal stratification in the liquid phase grows with increasing filling level. The vapor shows significant superheating while the liquid remains in a subcooled state, which is consistent with the experimental findings in the literature.

The obtained stratification profiles were found to be related to the flow structures due to natural convection. In particular, at low levels (10% and 20%) the circulations at the bottom of the tank result in better mixing of the liquid phase, which prevents thermal stratification from forming. In addition, increased average heat flux values to the liquid were obtained. However, the computed total heat ingress to the tank rises with increasing filling level.

Using lower insulation thicknesses for the tank results in an increased heat leak. This also leads to a rise in pressurization and boil-off rates, as well as higher velocities inside the tank. The relation among insulation thickness and heat ingress was established fitting the obtained values.

Further work should be conducted on addressing the effect of the thermal expansion of the liquid, which can influence self-pressurization, especially for large filling levels.

Acknowledgements

This work was partially supported by the Spanish Ministry of Science, Innovation and Universities through the Plan Nacional de I+D+i under grants MTM2015-68275-R and MTM2017-86459-R, the grant BES-2016-077228 and by FEDER and Xunta de Galicia funds under grant GRC GI-1563 ED431C 2017/60.

The authors also thank the Energylab Technology Center, with whom they collaborated during the initial stages of this work.

References

[1] BP, BP Energy Outlook 2019 Edition, https://www.bp.com/en/global/corporate/energy-economics/energy-outlook.html (2019).

[2] International Energy Agency (IEA), World Energy Outlook 2018, https://www.iea.org/weo2018/ (2018).

[3] G. Biscardini, R. Schmill, A. Del Maestro, Why small-scale LNG may be the next big wave, PWC, 2017.

[4] D. Dobrota, B. Lalić, I. Komar, Problem of boil-off in LNG supply chain, Trans. Marit. Sci. 2 (02) (2013) 91–100.

[5] E. Adom, S. Z. Islam, X. Ji, Modelling of boil-off gas in LNG tanks: A case study, Int. J. Eng. Technol. 2 (4) (2010) 292–296.

[6] L. A. Pellegrini, S. Moioli, F. Brignoli, C. Bellini, LNG technology: the weathering in above-ground storage tanks, Ind. Eng. Chem. Res. 53 (10) (2014) 3931–3937.

[7] M. F. Hasan, A. M. Zheng, I. Karimi, Minimizing boil-off losses in liquefied natural gas transportation, Ind. Eng. Chem. Res. 48 (21) (2009) 9571–9580.

[8] S. Gursu, S. Sherif, T. Veziroglu, J. Sheffield, Analysis and optimization of thermal stratification and self-pressurization effects in liquid hydrogen storage systems -— part 1: model development, J. Energy Res. Technol. 115 (1993) 221–227.

[9] M. Kang, J. Kim, H. You, D. Chang, Experimental investigation of thermal stratification in cryogenic tanks, Exp. Therm. Fluid Sci. 96 (2018) 371–382.

[10] M. Seo, S. Jeong, Analysis of self-pressurization phenomenon of cryogenic fluid storage tank with thermal diffusion model, Cryogenics 50 (9) (2010) 549–555.

[11] S. Das, S. Chakraborty, P. Dutta, Studies on thermal stratification phenomenon in LH2 storage vessel, Heat Transf. Eng. 25 (4) (2004) 54–66.

[12] M. S. Zakaria, K. Osman, M. N. A. Saadun, M. Z. A. Manaf, M. Hanafi, M. Hafidzal, Computational simulation of boil-off gas formation inside liquefied natural gas tank using evaporation model in ANSYS Fluent, in: Applied Mechanics and Materials, Vol. 393, Trans Tech Publ, 2013, pp. 839–844.

[13] S. Roh, G. Son, G. Song, J. Bae, Numerical study of transient natural convection in a pressurized LNG storage tank, Appl. Therm. Eng. 52 (1) (2013) 209–220.

[14] S. Barsi, M. Kassemi, Numerical and experimental comparisons of the self-pressurization behavior of an LH2 tank in normal gravity, Cryogenics 48 (3) (2008) 122–129.

[15] N. Van Dresar, C. Lin, M. Hasan, Self-pressurization of a flightweight liquid hydrogen tank: Effects of fill level at low wall heat flux, NASA TM 105411 (1992).

[16] S. P. Kumar, B. Prasad, G. Venkatarathnam, K. Ramamurthi, S. S. Murthy, Influence of surface evaporation on stratification in liquid hydrogen tanks of different aspect ratios, Int. J. Hydrogen Energy 32 (12) (2007) 1954–1960.

[17] J.-J. Ren, J.-Y. Shi, P. Liu, M.-S. Bi, K. Jia, Simulation on thermal stratification and destratification in liquefied gas tanks, Int. J. Hydrogen Energy 38 (10) (2013) 4017–4023.

[18] J. Shi, M. Bi, X. Yang, Experimental research on thermal stratification of liquefied gas in tanks under external thermal attack, Exp. Therm. Fluid Sci. 41 (2012) 77–83.

[19] J. Ren, H. Zhang, M. Bi, J. Yu, S. Sun, Numerical investigation of the coupled heat transfer of liquefied gas storage tanks, Int. J. Hydrogen Energy 42 (38) (2017) 24222–24228.

[20] J. H. Lee, Y. J. Kim, S. Hwang, Computational study of LNG evaporation and heat diffusion through a LNG cargo tank membrane, Ocean Eng. 106 (2015) 77–86.

[21] S. W. Choi, H. S. Kim, W. I. Lee, Analysis of leaked LNG flow and consequent thermal effect for safety in LNG cargo containment system, Ocean Eng. 113 (2016) 276–294.

[22] A. Saleem, S. Farooq, I. A. Karimi, R. Banerjee, A CFD simulation study of boiling mechanism and BOG generation in a full-scale LNG storage tank, Comput. Chem. Eng. 115 (2018) 112–120.

[23] M. Kulitsa, D. A. Wood, LNG rollover challenges and their mitigation on Floating Storage and Regasification Units: New perspectives in assessing rollover consequences, J. Loss Prevent. Proc. 54 (2018) 352–372.

[24] E. W. Lemmon, M. O. McLinden, D. G. Friend, Thermophysical properties of fluid systems, in: P. Linstrom, W. Mallard (Eds.), NIST Chemistry WebBook, NIST Standard Reference Database

Number 69, National Institute of Standards and Technology, Gaithersburg MD, 20899. doi:https://doi.org/10.18434/T4D303.

[25] A. Hofmann, The thermal conductivity of cryogenic insulation materials and its temperature dependence, Cryogenics 46 (11) (2006) 815–824.

[26] NIST Cryogenics Technology Group, 304 stainless steel material properties, https://trc.nist.gov/cryogenics/materials/304Stainless/304Stainless_rev.htm.

[27] Perlite Institute, Inc., Physical Characteristics of Perlite, https://www.perlite.org/wp-content/uploads/2018/03/physical-characteristics-perlite.pdf (2011).

[28] H. Enayati, A. J. Chandy, M. J. Braun, Numerical simulations of transitional and turbulent natural convection in laterally heated cylindrical enclosures for crystal growth, Numer. Heat Tr. A-Appl. 70 (11) (2016) 1195–1212.

[29] F. R. Menter, Two-equation eddy-viscosity turbulence models for engineering applications, AIAA J. 32 (8) (1994) 1598–1605.

[30] D. Wilcox, Turbulence modeling for CFD, Vol. 2, DCW industries La Cañada, CA, 1998.

[31] F. R. Menter, M. Kuntz, R. Langtry, Ten years of industrial experience with the sst turbulence model, Turbul. Heat Mass Transf. 4 (1) (2003) 625–632.

[32] ANSYS, Inc, ANSYS® Fluent, Release 19.0, Theory guide, ANSYS, Inc.

[33] C. W. Hirt, B. D. Nichols, Volume of fluid (VOF) method for the dynamics of free boundaries, J. Comput. Phys. 39 (1) (1981) 201–225.

[34] H. K. Versteeg, W. Malalasekera, An introduction to computational fluid dynamics: the finite volume method, Pearson Education, 2007.

[35] D. Sun, J. Xu, Q. Chen, Modeling of the evaporation and condensation phase-change problems with Fluent, Numer. Heat Tr. B-Fund. 66 (4) (2014) 326–342.

[36] C. Fang, M. David, A. Rogacs, K. Goodson, Volume of fluid simulation of boiling two-phase flow in a vapor-venting microchannel, Front. Heat Mass Transf. (FHMT) 1 (1) (2010) 013002.

[37] Y. Li, R. Wang, C. Wang, Study on effect of liquid level on the heat leak into vertical cryogenic vessels, Cryogenics 50 (6-7) (2010) 367–372.